

NUMERICAL STUDY OF THE REYNOLDS NUMBER EFFECT ON LOW ASPECT RATIO WINGS AT LOW SPEED

Dongyoun Kwak*, **Michele Gaffuri****, **Keisuke Ohira*****, **Joël Brezillon****

***Japan Aerospace Exploration Agency, **German Aerospace Center,**

*****Ryoyu Systems Co., Ltd.**

kwak.dongyoun@jaxa.jp; michele.gaffuri@dlr.de; ohirak@chofu.jaxa.jp; joel.brezillon@dlr.de

Abstract

Numerical studies were performed to understand the Reynolds number effect at high angle of attack and low-speed flight conditions for a supersonic aircraft configuration for which complex vortical flow dominates the overall flow field. To improve the simulation fidelity, dependency of the grid and the flow solver were surveyed. The characteristics of the turbulence modeling were also investigated by using several versions of the SA, $k-\omega$ SST and RSM models. The eddy viscosity significantly influences the vortex behavior at high angles of attack. With increasing Reynolds number, no obvious change of the flow field was observed at low angle of attack where the flow is mostly attached. However, the flow field was significantly changed at high angle of attack where the vortical flow dominates.

1 Introduction

Supersonic flight poses serious challenges to aircraft designers since the requirement for the supersonic cruise part of the flight are completely different from those for the slow take-off and landing part [1]. Recently, it has become clear that specialized tools are needed to help the designer meet this conflicting requirements by finding a solution that is satisfying both in terms of cruise fuel consumption and low speed performances. High fidelity tools like computational fluid dynamics (CFD) and computational structural mechanics (CSM) are deemed necessary to perform this job, since lower fidelity methods do not take into account phenomena that are important for such

a design work (e.g. vortex dominated flows, sonic boom and Reynolds number effect assessments).

In 2010 the Japan Aerospace Exploration Agency (JAXA) and the German Aerospace Center (DLR) have started cooperating in the field of supersonic transport aircraft research with the aim of improving their flow prediction and optimization tools in terms of capabilities, accuracy, and speed. Although the 2 partners' have different focuses, a thriving collaboration has taken place.

JAXA's main objective in the cooperation is to improve the fidelity of the CFD prediction of Reynolds number (Re) effects at high angle of attack (α) flight conditions. For the low speed and high α flight conditions, vortical structures are formed over the wing and their behavior strongly influences the aerodynamic characteristics [2]. For this kind of flow field, the Reynolds number effect is one of the important factors to be taken into account in order to accurately predict the aerodynamics for the flight conditions [3]. JAXA has put much effort to clarify Reynolds number effects, as well as to establish the computational tools that can accurately simulate the high Reynolds number flight conditions in this research.

DLR's main objective is to improve the capabilities of its aerodynamic optimization process in such a way that complex aircraft configurations (e.g. wings with deployed high-lift devices, engine integration cases) can be more easily treated. In essence this means developing an unstructured mesh generation process capable of delivering high quality meshes whose number of points is compatible with an optimization environment. Accuracy

and speed are of course in conflict with each other, so a trade-off between mesh size and accuracy has to be found. The simulation of the vortex-dominated flow past a delta wing in high lift conditions is a very demanding CFD application, and thus provides a good test case for the validation of the process.

In the strategy of the cooperation, a relatively simple geometry consisting of wing and fuselage (DLR-LOSLARW) is used in the first phase, and a complex geometry (JAXA-QsST) which includes tails and engine nacelles is selected in the second phase. The numerical research carried out in the first phase is the focus of the present paper. The characteristics of the turbulence models, computational grids and flow solvers were deeply investigated by comparing with experimental results and reference CFD solutions.

2 Reference geometry and Data

2.1 Low Aspect Ratio Wing Geometry

The Low Speed-Low Aspect Ratio Wing (LOSLARW) is a double delta wing-fuselage configuration with blunt wing leading edge (Fig.1). It features 4 deflected hinged-nose leading edge flaps. Previous studies have shown that these connections between flaps do not alter significantly the global aerodynamic behavior of the wing [4] and have the advantage of reducing the grid points needed to perform a CFD analysis while at the same time reducing the model manufacturing cost for the wind tunnel studies.

The geometry originates from the European project EPISTLE [5], in which the partners' objective was to design optimal high-lift leading

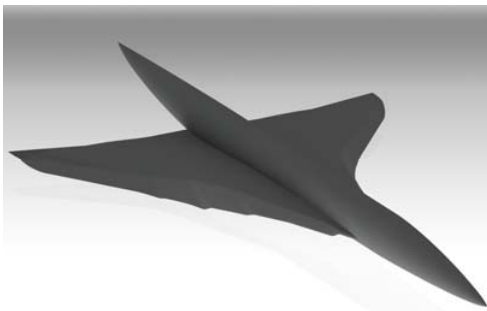


Fig.1 LOSLARW geometry

edge devices for a supersonic, Concorde size wing-body configuration. The optimal geometry obtained by DLR is here retained in the frame of the collaboration.

2.2 Reference Data

The experimental data obtained during the EPISTLE project could not be shared with JAXA. It was therefore agreed to use other reference data, obtained either from additional wind tunnel tests at low Reynolds number or through CFD computations on a grid well validated for high Reynolds flow conditions

2.2.1 Experimental results

Experimental data have been collected during a wind tunnel test campaign performed at the DNW-NWB wind tunnel facility in Braunschweig (Germany) using a closed test section. The 1:22 scaled model has a mean aerodynamic chord of 1.25 m and a wing area of 1.81 m². Experimental data are available for 2 Reynolds numbers (5.0×10^6 and 6.5×10^6) and consist of forces and moments as well as surface pressure values for certain wing and leading edge devices' locations. Additionally, oil flow pictures have been taken for selected cases.

2.2.2 Reference CFD solutions

For flight Reynolds number conditions where no experimental data are available, CFD computations on a hexahedral mesh have been used instead. The mesh has 4.2 million points and follows the guidelines developed in Ref.6. During the EPISTLE project, it was demonstrated that the CFD computations on this mesh are in good agreement with wind tunnel

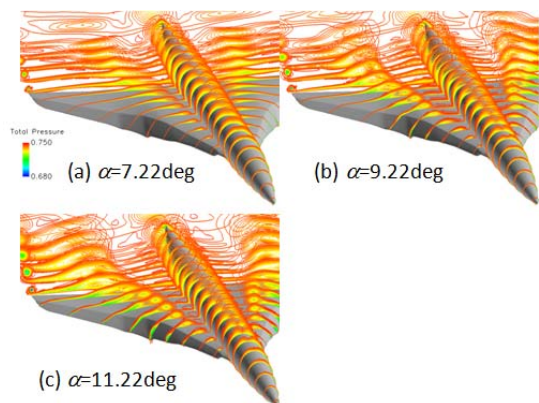


Fig. 2 Total pressure distributions obtained by the reference CFD solutions ($Re=22.5M$)

data at flight Reynolds number. Typical discrepancy between Wind Tunnel Data and CFD is within 4% in terms of drag values.

The computations are performed with the DLR-TAU solver (see section 3.2) using the RSM turbulence model. When a satisfying convergence of the residuals, or of the forces, could not be ensured with this high order turbulence model, the more stable $k-\omega$ SST model of Menter was used instead. Three sets of angles of attack and Reynolds numbers have been computed:

- $Re = 5.0 \times 10^6, 6.5 \times 10^6, 22.5 \times 10^6$
- $\alpha = 7.22^\circ, 9.22^\circ, 11.22^\circ$

Mach numbers for these simulations correspond to the ones used in the wind tunnel for the low Reynolds cases ($M=0.187$ and $M=0.232$ for $Re=5.0$ M, $Re=6.5$ M, respectively), while for the high Reynolds computations a free stream Mach number value of 0.25 has been chosen. The same mesh topology has been used, but meshes for different Reynolds number differ in the size of the first few layers off the wall, where a y^+ value of 1 has been used as guideline for the mesh generation.

Figure 2 shows the overall flow features at three angles of attack that were obtained by the reference CFD computations. At $\alpha=7.22^\circ$, attached flow is obtained all over the wing except for a weak vortex formed from the wing-fuselage intersection. With increasing α to 11.22° , complicate vortex behaviors are observed. Multiple vortices are formed from the nose-down flap, and those merge to a strong inboard vortex. It is evident that the overall flow field on the LOSLARW configuration is dominated by the attached flow at low α and by the vortical flow at high α .

3 Numerical Simulations

3.1 JAXA CFD Solvers

The main solver used in this research is the AeroDynamic Computational System (*ADCS*) solver, which is a compressible Euler and Reynolds-averaged Navier-Stokes (RANS) solver for multi-block structured grid [7]. *ADCS* uses a finite differential method and the third-

order TVD scheme of Chakravarthy-Osher for the convection terms, central difference for viscosity terms, and a diagonalized implicit method LU-ADI for time integration. In a previous study, the *ADCS* computations were validated on several flow fields at low speed and high alpha over a supersonic transport configuration [8]. To crosscheck the *ADCS* solver results, computations using the *UPACS* (Unified Platform for Aerospace Computational Simulation) solver were also conducted [9]. The *UPACS* uses a finite volume discretization method. The third-order Roe's flux difference splitting for convection terms with MUSCL extrapolation is chosen for the convection terms. And the Matrixfree Gauss Seidel method was used for time integration.

3.2 DLR CFD Solver

The DLR-TAU flow solver [10] is an unstructured, finite volume CFD solver. It solves the Euler or Navier-Stokes equations in RANS, LES, or hybrid RANS/LES mode. The (steady or unsteady) RANS equations can be closed using a number of different turbulence models, ranging from 1 equation models (Spalart-Allmaras and several derivatives) to more advanced second order closure models (Reynolds Stress models). The equations are advanced in time using an explicit multi stage Runge-Kutta scheme or an implicit Backward Euler scheme (solved using a LU-SGS approach), while the spatial derivatives are discretized using first/second order upwind schemes or a central second order scheme with artificial (scalar or matrix) dissipation. Additionally other advanced, state of the art, features are available, like grid deformation and refinement, treatment of chimera grids and resolution of the flow adjoint equation

3.3 CFD Validations

3.3.1 Flow solvers

As a first step in this study a comparison of the CFD codes is conducted in order to determine if the various solvers used in the project give similar results. This task is performed on a fine hexahedral mesh (25.8

million points) constructed by JAXA. Care is taken to use similar settings wherever possible, and especially for the turbulence modeling. Three CFD codes were used in this comparison; 1) *ADCS*: finite differences and structured grid computation, 2) *UPACS*: finite volume and structured grid, 3) *TAU*: finite volume and unstructured grid. The $k-\omega$ SST model is selected here; the details of the turbulence model were slightly different. The *ADCS* and *UPACS* respectively used the version of SST-V and SST, the *TAU* used the SST-2003 version [11].

Figure 3 shows the surface static pressure coefficient C_p distributions obtained by the three solvers and the reference solutions at $Re=22.5M$. The agreement between *ADCS* and *TAU* at $\alpha=7.22^\circ$ is good. However, at $\alpha=11.22^\circ$ there are small differences for the suction peak at $x/C=0.35$ and, $y/b=0.25$. These discrepancies were induced by the leading edge separation

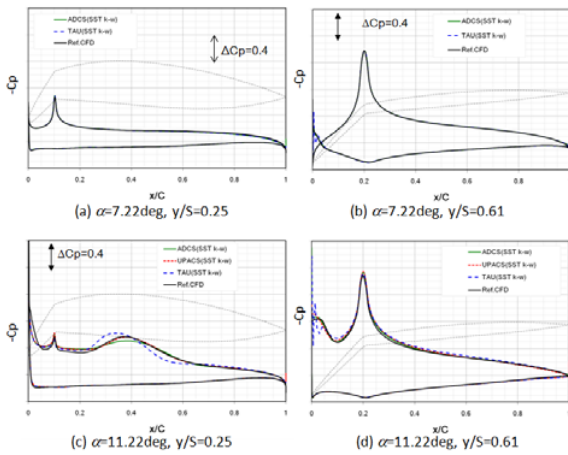


Fig.3 CFD solver comparison on the C_p distributions ($M=0.25$, $Re=22.5M$, SST k-w model)

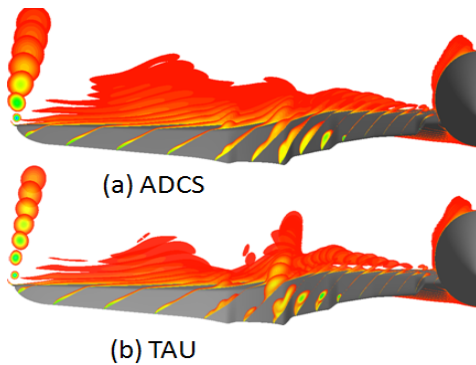


Fig. 4 Total pressure contours on some iso-x surfaces for the *ADCS* and *TAU* solutions.

Δ [$\times 10^{-4}$]	α [deg]	CL	CD	CDp	CDv	Cm
TAU-ADCS	7.22	1	-3	0	-3	-1
TAU-ADCS	11.22	15	-1	1	-2	-5
UPACS-ADCS	11.22	10	-3	-1	-2	-5

Table 1 Differences for each solver results at $Re=22.5M$ on the 25.8 M grid points

vortices; *TAU* seems to detect smaller flow details (Fig. 4). Relatively good agreement is obtained between the *UPACS* solutions and the reference solutions. A comparison of the aerodynamic loads predictions is shown in Table 1. The agreement in terms of forces and moments is remarkable, considering the difference between the solvers (structured versus unstructured, finite differences versus finite volumes). The 2 finite volume solvers (*UPACS*, *TAU*) predict higher C_L than the *ADCS* which uses a finite differences scheme.

3.3.2 Numerical grids

Firstly, the dependency of the grid density on the structured grid is surveyed using JAXA’s hexahedral grid, and secondly, the results on the hybrid type unstructured grids constructed by the DLR are studied.

Structured grids

The structured grid is comprised of 82 blocks, and the total number of grid points is 25.8 million (this is the grid called “fine” in the following) [12]. The height of the first grid off the surface is 2×10^{-3} mm, with a maximum $y+$ value of 2.0 (wall unit) on the $Re=22.5 \times 10^6$ case. The stretching of the spatial grid in the direction normal to the surface was carefully arranged to correctly capture the vortical structures. To validate the arrangement of the spatial grid, the grid dependency was surveyed by globally and isotropically refining and coarsening the grid (see Table 2). The aerodynamic forces obtained from several grid densities are plotted in Fig.5. The horizontal axis is a value of $N^{2/3}$ (N : grid points). The aerodynamic coefficients linearly

	Grid points [M]	Height of first grid [mm]
Coarse	7	0.0034
Medium	13.1	0.0027
Fine	25.8	0.002
Extra-Fine	58.6	0.0015

Table 2 The size of the structured grids

change with respect to $N^{-2/3}$. Aerodynamic

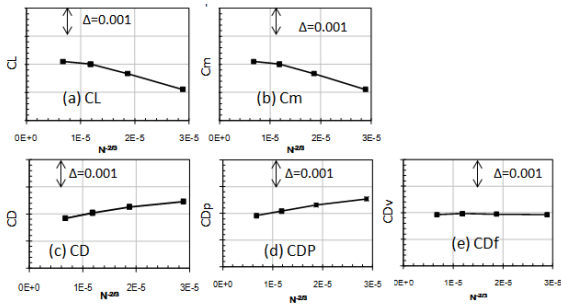


Fig.5 The grid dependency on the JAXA structured grid ($Re=22.5 \times 10^6$, $M=0.25$, $\alpha=11.22^\circ$)

forces on an ideally fine mesh ($N^{-2/3}=0$) are estimated by linear extrapolation following Richardson's method using two values at $N^{-2/3}=0.7 \times 10^{-5}$ ($N=58.6M$) and $N^{-2/3}=1.1 \times 10^{-5}$ ($N=25.8M$). The differences of the forces between $N^{-2/3}=0$ and $N^{-2/3}=1.1 \times 10^{-5}$ ($N=25.8M$) are smaller than $\Delta=0.0005$, and these values are typical reference values to determine the grid dependency at $Re=22.5M$. Since obvious discrepancies on the C_p distribution were not identified, the fine grid used in this research is reasonable for the assessment of the fidelity of the CFD tools.

Unstructured grids

Various meshes have been used on DLR side. Main task was to validate unstructured mesh approaches for vortex dominated flows [13]. The study has been performed using the Centaur [14] and Solar [15] mesh generators. Both unstructured meshes are of hybrid type: near the walls prismatic elements are extruded from the surface mesh to capture the boundary layer. Outside this layer the mesh is tetrahedral. The main difference between the 2 grids is the surface mesh: Centaur creates triangular surface

	Grid points [M]	Surf. points	Prismatic layers
Centaur	10.9	202347	40
Solar	11.5	314193	33

Table 3 The size of the unstructured grids

Δ [$\times 10^{-4}$]	CL	CD	CDp	CDv	Cmy
Centaur	1	0	0	2	16
Solar	3	3	4	0	2

Table 4 Difference between results on the unstructured meshes and the structured reference result ($Re=22.5M$, $M=0.25$, $\alpha=11.22^\circ$, $k-\omega$ turbulence model)

meshes, while Solar generates unstructured

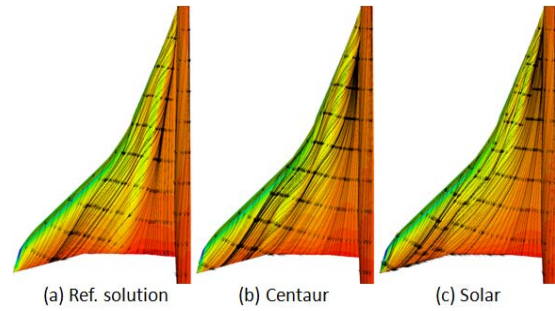


Fig. 6 Comparison of the wing's suction side pressure distribution and surface streamlines

quadrilateral grids. The latter has the advantage of being able to build (highly) anisotropic meshes thus saving some points. The major characteristics of the resulting meshes are outlined in Table 3.

Table 4 shows the difference, in absolute value, between the reference result on the reference structured mesh and results on the 2 unstructured meshes. The results are excellent for the forces. However the pitching moment coefficient shows significant discrepancy for the Centaur mesh result, suggesting a difference in the flow topology on the wing. This is confirmed by the pressure distribution and skin friction comparison: width and location of the main wing vortex differ between the 3 solutions (Fig.6). Moreover unstructured meshes are not capable of capturing the vortex as far downstream as the structured does. The flow topology however is globally captured by the unstructured meshes so that they can be used whenever a very accurate vortex resolution is not required.

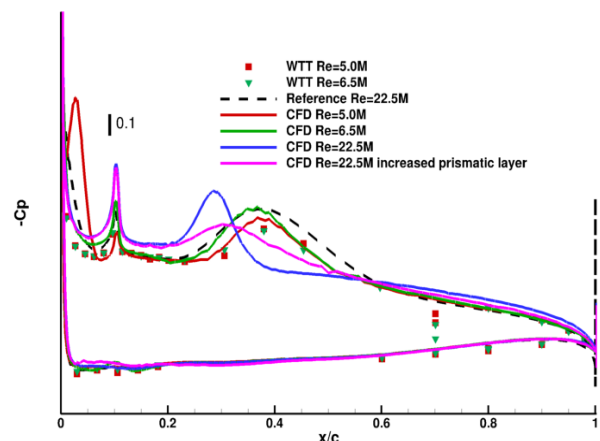


Fig. 7 C_p distribution on the section $y/S = 0.25$ for 3 Reynolds numbers. (Solar meshes, $\alpha=11.22^\circ$, TAU)

turbulence model	detail version	Ref. 20
<i>Spalart-Allmaras</i>	SA	SA-noft2
	SA-R	SA-noft2-R(Crot=1)
	SA-RC-A	SA-noft2-RC
	SA-RC-B	SA-noft2-RC(Cr3=0.3)
<i>k-ω SST</i>	SST	SST
	SST-V	SST-V
	SST-2003	SST-2003
	SST-VRC-A	SST-V-RC
	SST-VRC-B	SST-V-RC(Cr3=0.3)

Table 5 Version's name of the turbulence models

Figure 7 shows the pressure distributions on Solar meshes for various Reynolds numbers at Section 1. Wind tunnel data and reference CFD results are also plotted. Simulations at low Reynolds number are performed on a mesh with modified settings for the prismatic layer, to account for the increased boundary layer height. CFD results at low Reynolds are in good agreement with the experimental results, while the high Reynolds case shows some discrepancies with respect to the reference result in term of vortex location and suction peak intensity. It is argued that the thicker prismatic

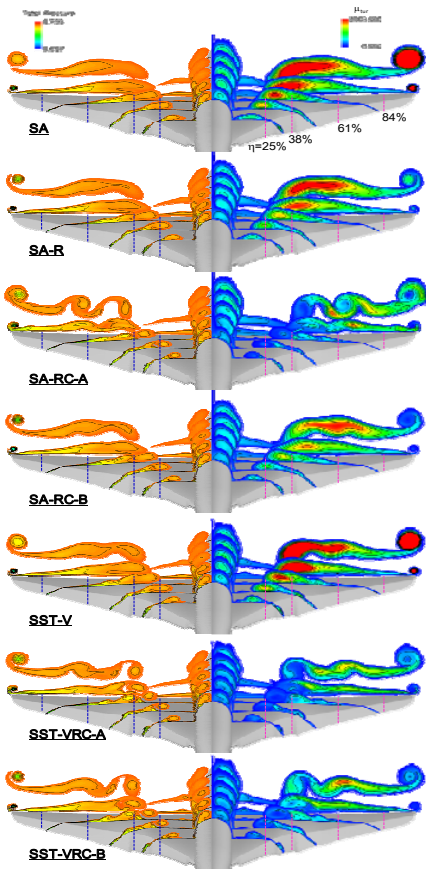


Fig.9 Overall flow features for several turbulence models ($Re=5M$, $\alpha=11.22^\circ$)

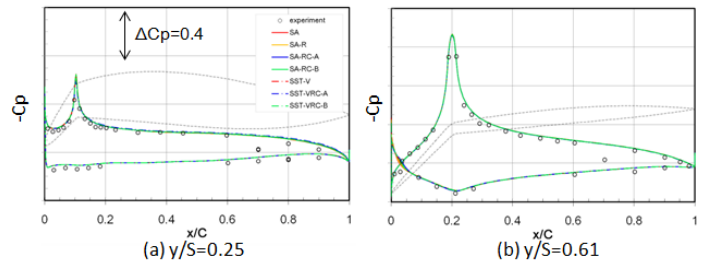


Fig.8 C_p distributions for several turbulence models ($Re=5M$, $\alpha=7.22^\circ$, ADCS)

layer in the low Reynolds cases mesh helps the capturing of the vortex. To verify this, a mesh with a greater prismatic layer thickness is used for the high Reynolds case. The result (purple line in Fig. 7) shows some improvement over the initial result, thus verifying the hypothesis.

3.3.3 Turbulence models

An important part of the validation work is the turbulence modeling study [12]. The characteristics of several turbulence models were compared using the ADCS code and the TAU code.

Standard versions of the two turbulence models (*SA*, *k- ω SST*) and several versions of each model (rotation correction, rotation curvature correction) for the fine structured grid (25.8M points) were used in this study [16-22]. Table 5 shows the short names of those versions and corresponding names suggested from Ref. 23 are also written here. Furthermore, the effects of the eddy viscosity were investigated by changing the strength of the rotation and streamline curvature effects on the rotation curvature correction (*SA-RC-B* in Table 5).

No obvious discrepancies due to the turbulence modeling were revealed from the C_p distributions at $\alpha=7.22^\circ$ (Fig.8). It means that the CFD computations can precisely predict the flow field where the attached flow dominates. On the other hand, Fig.9 shows the flow features obtained with several versions of the turbulence models at $\alpha=11.22^\circ$ and $Re=5M$. The total pressure distributions are plotted on the left hand side, while the eddy viscosity distributions are plotted on the right hand side. The vortical flow features differ significantly from version to version. Especially, high eddy viscosity areas are obtained at the inboard vortex with the SA model. This higher viscosity induces strong

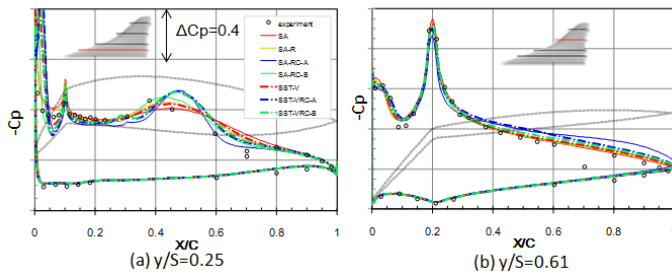


Fig.10 C_p distributions for several turbulence models ($Re=5M$, $\alpha=11.22^\circ$, ADCS)

dissipation of the vortex. However, for the *SA-RC-A* on which the eddy viscosity production was limited by the rotation curvature correction, multiple vortices are still observed near the trailing edge. The high eddy viscosity area of the *SA-RC-A* is drastically smaller than the area of the *SA*. Moreover, by controlling the strength of the rotation and streamline curvature effects with the parameter $C_{r3}=0.3$ (*SA-RC-B* version), the vortical flow features are drastically changed from *SA-RC-A*. Similar trend was also observed

on the $k-\omega$ SST models. The C_p distributions from several versions of the *SA* model are seen in Figure 10. The suction peaks induced by the inboard vortex are clearly observed at $x/C=0.5$ on $y/b=0.25$ for the *SA-RC-A*. These suction peaks disappear when using the original *SA* model, because vortical flow becomes weak by strong dissipation caused by the eddy viscosity. It is evident that the tuning of the eddy viscosity production can significantly change the vortical flow behavior.

A similar comparison of the turbulence modeling was conducted using the *TAU* solver. Three turbulence k models have been used: the *SA* model [16], the $k-\omega$ SST model [17], and a *RSM* model based on the Speziale-Sarkar-Gatski model in the field and on the Launder-Reece-Rodi near the walls [24]. The latter is a higher order method (7 equations), supposed to give better results than other models when dealing with complex flow situations. The computations are performed on the 4.2 million points structured mesh using the *TAU* solver.

In Fig. 11 results are shown in the C_L-C_D space. The *SA* model predicts higher drag levels compared to the other models. The likely cause is the higher pressure loss at the wing-fuselage intersection, as it can be seen in Fig.12. A difference in the forces between the $k-\omega$ SST and *RSM* models is only visible at $\alpha=9.22^\circ$. The vortical flow on the inboard leading edge flap differs slightly between the 2 solutions at this angle of attack, the *RSM* solution showing 2 vortical structures instead of 1 for $k-\omega$ SST (Fig. 12). Additionally, the vortex onset location differs slightly between these 2 models.

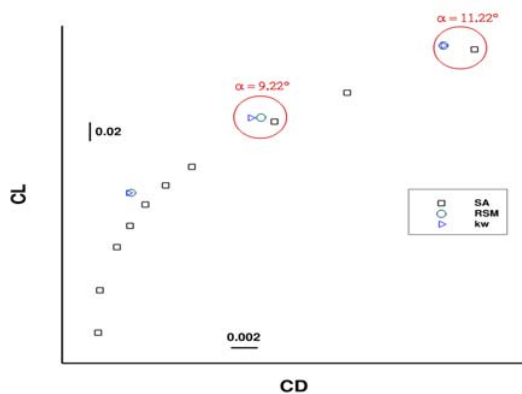


Fig.11 Polar at $Re=22.5M$, $M=0.25$ for the 3 turbulence models

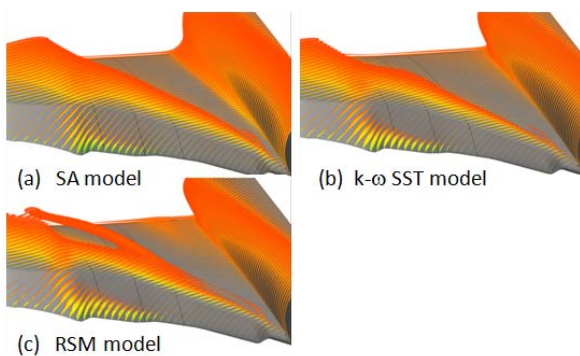


Fig.12 total pressure contours for the $Re=22.5$, $M=0.25$, $\alpha=9.22^\circ$ case

4 Reynolds number effects

Accurate prediction of the Reynolds number effects is the main aim of this research. Even though many issues remain unsolved, some results of the Reynolds number effects study are discussed in this chapter. The computations were conducted using the *ADCS* code with the *SST-V* turbulence model on JAXA's fine grid.

The C_p distributions at two Reynolds numbers ($Re=5M$, $22.5M$) at $\alpha=7.22^\circ$ are shown

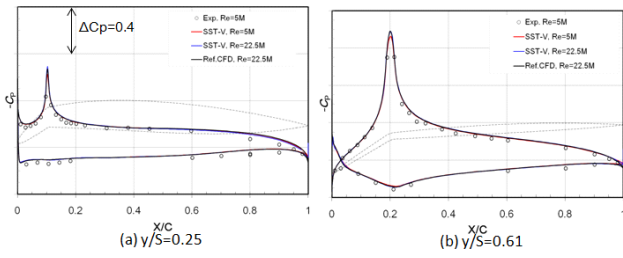


Fig. 13 Reynolds number effects on the C_p distribution ($\alpha=7.22^\circ$)

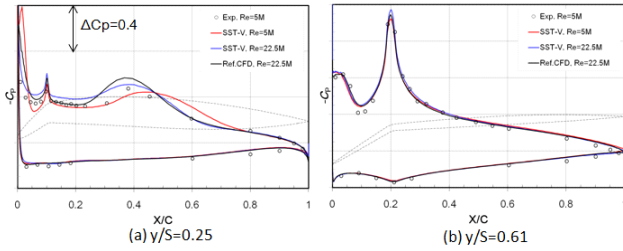


Fig. 14 Reynolds number effects on the C_p distribution ($\alpha=11.22^\circ$)

in Fig.13. The experimental results at $Re=5.0M$ and the reference CFD results at $Re=22.5M$ are also plotted to enhance the comparison. As mentioned in the previous section, the flow is attached for the entire wing surface at this low α . When the Re increases, smaller increments of C_p are only observed at the leading edge flap hinge locations. The boundary layer becomes

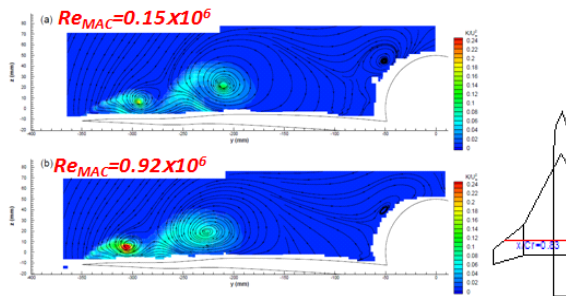


Fig.15 Re effects on turbulence kinematic energy ($\alpha=12^\circ$; ref.22)

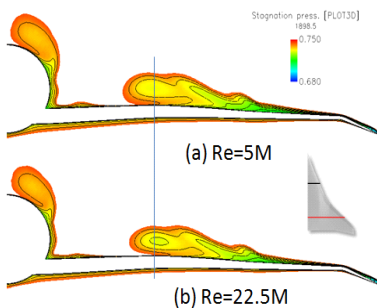


Fig.16 Spanwise total pressure distributions at different Re ($\alpha=11.22^\circ$)

thinner with increasing the Re . The further accelerated flow past the hinge at high Re induces higher C_p suction peaks.

C_p distributions at $\alpha=11.22^\circ$ are shown in Fig.14. The C_p at $y/b=0.25$ is significantly changed with increasing the Re . This effect is caused by the inboard vortex behavior. Watanabe, et. al. investigated the Re effects on the leading edge separation vortices over a cranked arrow wing configuration by means of PIV measurements [25]. They found that by increasing the Re , the location of the inboard vortex moves slightly outboard and closer to the wing surface (Fig. 15; Ref. 25). Figure 16 shows the total pressure distributions that correspond to the cases plotted in Fig.15. A behavior similar to Ref. 25 is also observable in this case for the location of the inboard vortex. The outward movement of the inboard vortex with increasing the Re induces the forward movement of the suction peak when the observation is conducted at a constant spanwise location ($y/b=0.25$). The Re effects obtained between the reference solutions ($Re=22.5M$) and the experimental results ($Re=5M$) show a similar trend. On the other hand, obvious difference of the C_p distributions between both Re is not obtained at the outboard wing (Fig.14 (b)).

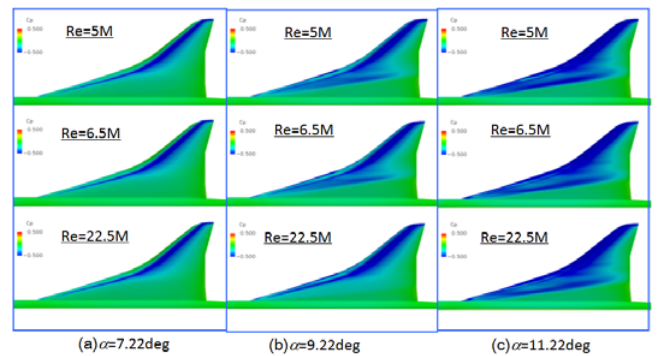


Fig. 17 Surface C_p distribution at three Re

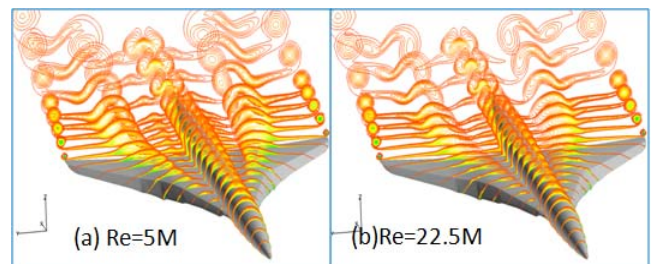


Fig. 18 Total pressure distribution ($\alpha=9.22^\circ$)

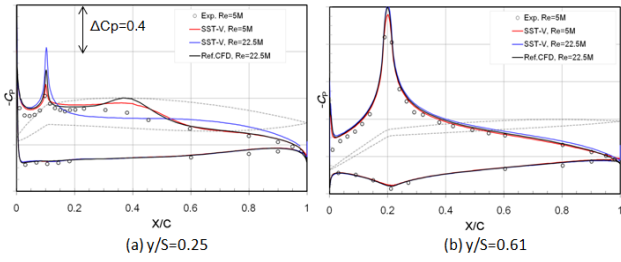


Fig. 19 Reynolds number effects on the C_p distribution ($\alpha=9.22^\circ$)

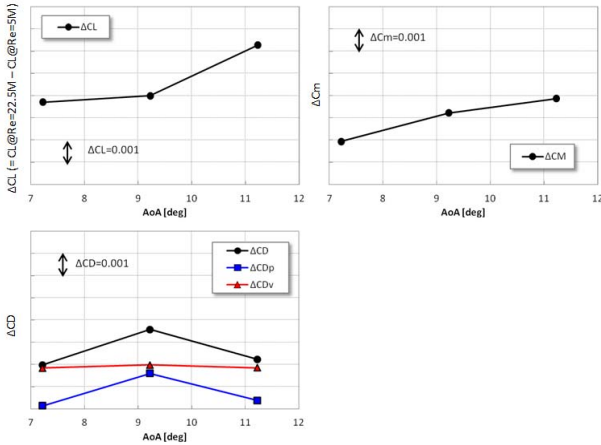


Fig. 20 Absolute value of the difference of the aerodynamic forces between $Re=22.5M$ and $Re=5M$

Figure 17 shows the C_p distributions over the upper wing at three angles of attack. Low pressure regions are observed at the inboard wing at $Re=5M$ and $6.5M$ and $\alpha=9.22^\circ$; these are similar to the results at $\alpha=11.22^\circ$ for three Re (Fig.17(c)). However, the suction area disappears at $Re=22.5M$ and $\alpha=9.22^\circ$, which shows a pattern similar to those obtained at $\alpha=7.22^\circ$ (Fig.17(a)). The disappearance of the suction area means that the effects of the inboard vortex decrease at high Re . This Re effects can be clearly seen in Fig.18, 19. With increasing the Re , C_L and the pitch-down moment C_m increase, while C_D decreases. Figure 20 shows the absolute value of the difference of the aerodynamic forces between $Re=22.5M$ and $Re=5M$. ΔC_L is the C_L increment by increasing Re ($\Delta C_L = C_L$ at $Re=22.5M - C_L$ at $Re=5M$). Similarly, ΔC_m is the increment of pitch-down direction component, and positive ΔC_D is the decrement of the C_D by increasing Re . The ΔC_D is divided in pressure drag component ΔC_{DP} and friction drag component ΔC_{DF} (Fig.

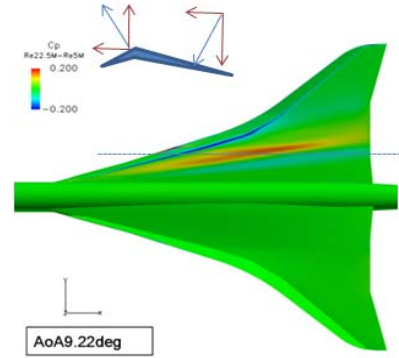


Fig. 21 Difference of the C_p between $Re=22.5M$ and $Re=5M$

20(c)). The ΔC_{DF} for the three α is similar. However, the ΔC_{DP} at $\alpha=9.22^\circ$ is obviously larger than other two α . Figure 21 shows the difference of the C_p distributions on the upper surface between $Re=22.5M$ and $Re=5M$ ($\Delta C_p = C_p$ at $Re=22.5M - C_p$ at $Re=5M$). A large area where the pressure increases with Re is visible over the inboard section while a negative pressure difference is observed at the leading edge flap. Both phenomena contribute to a reduction of C_D (which explains the high ΔC_{DP} value), while their effect on C_L is limited by the fact that the forces generated act in opposite directions (see sketch on Fig. 21). Similar observations can be made on the TAU solutions; this leads to the conclusion that $ADCS$ is able to predict the Re effects with reasonable accuracy.

From this study, it was clarified that the accurate simulation of the vortex behaviors at high α is very important to assess the Re effects with high fidelity. Similar trends were also obtained for the other turbulence models. However, the flow field at $\alpha=11.22^\circ$ where the vortical flow dominates was strongly dependent on the turbulence model and flow solver. Furthermore, the vortical flow is also influenced by the Re .

5 Conclusions

Numerical studies were performed to understand the Reynolds number effect at the high angles of attack typical of a supersonic aircraft configuration in low-speed flight conditions. To improve the simulation fidelity,

characteristics of the grid dependency, flow solver and turbulence modeling were surveyed.

- The vortex behavior at high angle of attack where vortical flow dominates the overall flow field is slightly dependent on the CFD method (structured versus unstructured, finite volume versus finite difference).
- The characteristics of the turbulence modeling were investigated by using several versions of the SA, $k-\omega$ SST and RSM models. The eddy viscosity significantly influences the vortex behaviors at high α . The modification of the rotation and streamline curvature effects by the rotation curvature correction promotes the vortex formation at the inboard leading edge, and limits the vortex dissipation during its transport downstream.
- With increasing Reynolds number, no obvious change of the flow field was obtained at low α where the flow is attached. On the contrary the flow field is significantly changed at high α where the vortical structures dominate. The vortex formation from the inboard wing is restricted by increment of the eddy viscosity in the boundary layer at higher Reynolds number.
- The unstructured grid are capable of estimating the aerodynamic loads with good accuracy, even though the vortical flow structures present some discrepancies compared to the reference solutions. Increasing the prismatic layer size mitigates the problem.

References

- [1] Antani, D.L. and Morgenstern, J.M. HSCT high-lift aerodynamic technology requirements. *AIAA paper* 92-4228.
- [2] Brennenstuhl U and Hummel D. Vortex Formation Over Double-Delta Wings, Proceedings of 13th Congress of the International Council of the Aeronautical Science (ICAS Paper 82-6.6.3), Seattle, USA, Aug. 1982, pp 1302-1309.
- [3] Ohnuki, T., Hirako, K., and Sakata, K., "National Experimental Supersonic Transport Project," *International Congress of the Aeronautical Science*, 2006-1.4.1, 2006.
- [4] Herrmann U., Low-Speed High-Lift Performance Improvements Obtained and Validated by the EC-Project EPISTLE, *24th International Congress of the Aeronautical Sciences*, ICASE-2004-411, August 29 - September 3, Yokohama, Japan.
- [5] Herrmann U., EPISTLE : High lift system design for low-noise applied to a supersonic aircraft, *Aeronautical Journal*, vol. 110, n.1107, pp. 327-331, 2006.
- [6] van Muijden J, Elsenaar B, Numerical prediction capabilities and analysis of flow development for a supersonic civil transport at low speed. *Proceedings of the CEAS Aerospace Aerodynamics Conference*, Cambridge, 10-12 June, 2002.
- [7] Lei, Z. Flow simulation of a supersonic transport configuration at low-speed and high-lift conditions. *Journal of Aircraft*, Vol.45, No.5, pp1514-1521, 2008.
- [8] Lei, Z., "Effect of RANS Turbulence Models on Computation of Vortical Flow over Wing-Body Configuration," *Trans. Japan Soc. Aero. Space Sci.* Vol.48, No.161, pp.152-160, 2005.
- [9] Takaki,R., Yamamoto,K. Ymane,T. Enomoto,S and Mukai,J., "The Development of the UPACS CFD Environment," *High Performance Computing*, Proc. of ISHPC 2003, Springer, pp.307-319, 2003
- [10] Schwamborn D., Gerhold T., Heinrich R., The DLR TAU-Code: Recent Applications in Research and Industry, *ECCOMAS CFD 2006*, Egmond aan Zee, the Netherlands, 2006.
- [11] Menter F.R., Kuntz M, Langtry R., „Ten Years of Industrial Experience with the SST Turbulence Model“, *Turbulence, Heat and Mass Transfer 4* (2003)
- [12] Ohira, K., Kwak, D., Brezillon, J. and Gaffuri, M., "Numerical Study of the Eddy Viscosity Turbulence Model for High Alpha Flow over the Low Aspect Ratio Wing", 44th Fluid Dynamics Conference/Aerospace Numerical Simulation Symposium 2012, Toyama, Japan, 2012 (in Japanese).
- [13] Gaffuri, M., Brezillon, J. "Unstructured Mesh Capabilities for Supersonic Wing Design at Low Speed Conditions", *ECCOMAS CFD and Optimization Thematic Conference*, Antalya, 2011.
- [14] Centaursoft, <http://www.centaursoft.com>
- [15] D. G. Martineau D.G., Stokes S., Munday S. J., Jackson A. P., Gribben B. J., "Anisotropic Hybrid Mesh Generation for Industrial RANS Applications", *AIAA-paper 2006-534*, AIAA Aerospace Conference, Reno, USA (2006).
- [16] Spalart P. R., Allamaras S. R., A One-Equation Turbulence Model for Aerodynamic Flows, *AIAA Paper* 92-0439, 1992.
- [17] Menter F. R., Two-Equation Eddy Viscosity Turbulence Models for Engineering Applications, *AIAA Journal*, Vol. 32, No.8, pp. 1598-1605, 1994.
- [18] Spalart, P. R., Shur, M. L., "On the Sensitization of Turbulence Models to Rotation and Curvature", *Aerospace Science and Technology*, Vol.1, No.5, 1997, pp.297-302.
- [19] Smirnov, P. E., Menter, F. R., "Sensitization of The SST Turbulence Model to Rotation and Curvature by

- Applying the Spalart-Shur Correction Term,” ASME GT2008-50480, 2008.
- [20] Dacles-Mariani, J., Zilliac, G. G., Chow, J. S., Bradshaw, P. “Numerical/Experimental Study of a Wingtip Vortex in the Near Field,” AIAA Journal Vol.33, No.9, Sep. 1995, pp. 1561-1568.
- [21] Shur, M. L., Strelets, M. K., Travin, A. K., Spalart, P. R. “Turbulence Modeling in Rotating and Curved Channels: Assessing the Spalart–Shur Correction,” AIAA Journal Vol.38, No.5, May, 2000, pp.784-792.
- [22] Monson, D. J., Seegmiller, H. L., McConnaughey, P. K., Chen, Y. S., “Comparison of Experiment with Calculations Using Curvature-Corrected Zero and Two Equation Turbulence Models for a Two-Dimensional U-Duct” AIAA Paper 90-1484, Jun. 1990.
- [23] Rumsey, C. L., Smith, B. R., Huang, G.P., “Description of a Website Resource for Turbulence Modeling Verification and Validation,” AIAA Paper 2010-4742, Jun. 2010.
- [24] Eisfeld B., Brodersen O., Advanced Turbulence Modelling and Stress Analysis for the DLR-F6 Configuration, *AIAA-Paper* 2005-7727, 2005.
- [25] Watanabe S, Kato H, Kwak D Y, Shirotake M and Rinoie K. Stereo PIV Measurements of Leading Edge on a Cranked Arrow Wing, *Measurement Science and Technology*, Vol.15, No.6, 2004, pp1079-1089.

Copyright Statement

The authors confirm that they, and/or their company or organization, hold copyright on all of the original material included in this paper. The authors also confirm that they have obtained permission, from the copyright holder of any third party material included in this paper, to publish it as part of their paper. The authors confirm that they give permission, or have obtained permission from the copyright holder of this paper, for the publication and distribution of this paper as part of the ICAS2012 proceedings or as individual off-prints from the proceedings.